Theoretical Description of Pump-Probe Experiments in Charge-Density-Wave Materials out to Long Times

Marko D. Petrović,[1] Manuel Weber,[2,3] and James K. Freericks[1,*]

[1]*Department of Physics, Georgetown University, Washington, DC 20057, USA*

[2]*Max Planck Institute for the Physics of Complex Systems, Nöthnitzer Strasse 38, 01187 Dresden, Germany*

[3]*Institut für Theoretische Physik and Würzburg-Dresden Cluster of Excellence ct.qmat, Technische Universität Dresden, 01062 Dresden, Germany*

(Received 4 December 2022; revised 24 November 2023; accepted 8 July 2024; published 25 September 2024)

We describe coupled nonequilibrium electron-phonon systems semiclassically—Ehrenfest dynamics for the phonons and quantum mechanics for the electrons—using a classical Monte Carlo approach that determines the nonequilibrium response to a large pump field. The semiclassical approach is expected to be accurate, because the phonons are excited to average energies much higher than the phonon frequency, eliminating the need for a quantum description. The numerical efficiency of this method allows us to perform a self-consistent time evolution out to very long times (tens of picoseconds), enabling us to model pump-probe experiments of a charge-density-wave (CDW) material. Our system is a half-filled, one-dimensional (1D) Holstein chain that exhibits CDW ordering due to a Peierls transition. The chain is subjected to a time-dependent electromagnetic pump field that excites it out of equilibrium, and then a second probe pulse is applied after a time delay. By evolving the system to long times, we capture the complete process of lattice excitation and subsequent relaxation to a new equilibrium, due to an exchange of energy between the electrons and the lattice, leading to lattice relaxation at finite temperatures. We employ an indirect (impulsive) driving mechanism of the lattice by the pump pulse due to the direct driving of the electrons. We identify two driving regimes, where the pump can either cause small perturbations or completely invert the initial CDW order. Our work successfully describes the ringing of the amplitude mode in CDW systems that has long been seen in experiment but never successfully explained by microscopic theory. We also describe the fluence-dependent crossover that inverts the CDW order parameter and changes the phonon dynamics. Finally, we illustrate how this method can examine a number of different types of experiments including photoemission, x-ray diffraction, and two-dimensional (2D) spectroscopy.

DOI: 10.1103/PhysRevX.14.031052 Subject Areas: Condensed Matter Physics

I. INTRODUCTION

A variety of experimental techniques exist to track nonequilibrium dynamics in excited condensed matter systems, for example, time- and angle-resolved photoemission spectroscopy (trARPES), ultrafast electron diffraction, time-resolved x-ray diffraction, or transient optical spectroscopy. Through the application of these techniques, it becomes possible to explore and possibly control new states of matter created in pump-probe experimental settings. Time-resolved angle-resolved photoemission spectroscopy is an ultrafast measuring technique [1–4] capable of capturing the real-time evolution and occupation of electronic states in an array of materials: from superconductors [5] and semimetals such as graphene [6] to topological insulators [7]. A particular focus is given to charge-density-wave (CDW) materials [8,9] due to the specific ordering nature of their ground state and different competing phases they can exhibit. The trARPES experiments utilize a combination of time-delayed pump and probe pulses to excite the studied material and track the dynamics of the induced nonequilibrium state. The technique was so far successfully used to study oscillations of the CDW amplitude mode, as well as CDW melting in various materials, from TaS_2 [10,11] to rare-earth tritellurides such as $TbTe_3$ [12–14], $LaTe_3$ [15], and $DyTe_3$ [16]. Photoinduced insulator-to-metal phase transitions and charge order melting was also measured in quasi-1D

*Contact author: James.Freericks@georgetown.edu

organic salts using time-resolved optical spectroscopy [17]. Additionally, photoemission spectroscopy was used to study the dynamics of the electronic structure out of equilibrium in the quasi-1D CDW material blue bronze [18].

In a typical trARPES experiment, the pump-induced modification of the electronic structure is observed in the measured photoemission spectrum (PES). The lattice can be driven due to direct dipole coupling with the pump field or indirectly through coupling with electrons. The conventional explanation of the indirect driving involves the transfer of energy from the laser pump to electrons, happening on a femtosecond timescale, and then from electrons to the crystal lattice, happening on a picosecond timescale. A detailed understanding of this driving mechanism is essential in the context of Floquet engineering [19], where the dressing of the electronic structure by lattice motion can be used to fine-tune the electronic spectrum.

In addition to trARPES, which focuses on the electronic spectrum, it is also useful to examine nonequilibrium structural dynamics via ultrafast diffraction [20]. One can use ultrafast electron diffraction or ultrafast x-ray diffraction [21]. Some recent diffraction studies explored lattice motion in tritellurides [22–24] and dichalcogenides [25].

The theoretical description of pump-probe experiments for CDW systems has relied on phenomenological approaches like time-dependent Ginzburg-Landau theory, whereas the study of microscopic models has been hindered by the absence of efficient numerical methods that can resolve the very different timescales of electron and phonon dynamics. Dynamical mean-field theory [26,27] and related studies [28–30] focused on the excitation of the nonequilibrium electronic state for several tens of femtoseconds, but the slow lattice motion was not considered. But, within this short time frame, many different types of experiments have been examined, including nonequilibrium resonant inelastic x-ray scattering spectra [31] in an approach that ignores the momentum dependence of the resonant inelastic x-ray scattering response. Exact diagonalization and the density-matrix renormalization group are alternative methods subject to different limitations, such as small lattice sizes, short timescales, or high phonon frequencies [32–37]; as time proceeds, the growing number of phonon excitations and the growing entanglement of the quantum state often make it difficult to run simulations for long times, although local basis optimization (and other strategies) can mitigate this issue. To date, density-matrix renormalization group calculations have focused only on high phonon frequencies (eV range) rather than phonon frequencies in the meV range, which are required for an accurate description of most CDW materials. A closely related approach to pump-probe experiments with impulsively driven phonons is the theory of displacive excitation of coherent phonons [38]. In this theory, the equilibrium coordinates of the lattice phonons (that have the same symmetry as the lattice) have their quasiequilibrium position displaced proportional to the change in the charge density of the electrons due to the pump excitation. While this interpretation is different from the electron-phonon coupling approach we use here (because we impulsively drive the phonons), the semiclassical equations of motion are essentially identical, each having a force term proportional to the change in the electron density. Note that, in our work, we do not need to add a damping term, as that automatically arises in our formalism for nonzero temperature initial states. To explain the indirect driving mechanism, as exemplified by the experiment in Ref. [12], it is necessary to develop approaches that naturally include the slow phonon dynamics.

In this article, we extend a time-dependent Monte Carlo (MC) method [39], recently developed for frozen phonons, to include the classical lattice motion. This approach is similar to that of *ab initio* molecular dynamics [40], except we can also examine measurable electronic properties in the context of trARPES experiments. A classical description of the phonons is expected to become accurate if the temperature and/or the Peierls gap are larger than the phonon frequency [41], as confirmed by exact quantum Monte Carlo simulations in equilibrium [42]. For realistic parameters, this is already the case at very low temperatures. Although the semiclassical approach is poor at zero temperature, because it neglects the quantum fluctuations in the ground state and has no damping, we find that a sliding time average of $T = 0$ data can still explain some of the features we observe at finite temperatures. Furthermore, the addition of energy into the system via a strong pump only improves the accuracy of this method, as the quantization of the phonon energies becomes less and less important. For our method to be efficient, we neglect electron-electron interactions, as they mainly affect the short-time decay after the pump. The present method captures the universal long-time features of the induced lattice dynamics. In particular, our results reveal details of the indirect driving mechanism found in experiments. Note, however, that this approach cannot describe superconductivity, because superconductivity requires dynamical quantum phonons. So this approach is limited to CDW phases and thermally induced disordered phases.

Although in this paper we treat phonons classically using Ehrenfest forces, our method should not be confused with the methods widely used in quantum chemistry. The dynamics in small molecular systems can often be described with just a few well-defined potential energy surfaces. This leads to combined quantum-classical approaches such as multitrajectory Ehrenfest (MTE) or fewest-switches surface hopping (FSSH) methods [43,44]. However, in a solid (due to a large number

of constituent atoms), the density of different energy surfaces per unit of energy increases with the system size to a point where problematic surface crossings become unavoidable. Another obstacle is related to modeling the interaction of the pump field with the electronic system which dresses the electronic structure (and the potential energy surfaces), making the traditional chemistry-based approaches virtually impossible for solids. We discuss the similarities and differences between our approach and MTE and FSSH later in a separate subsection.

Before explaining our method, we briefly describe the Holstein model and summarize our main findings. A simplified schematic of a trARPES setup (to which we apply our method) is shown in Fig. 1(a). In equilibrium at zero temperature, it is a perfectly dimerized tight-binding chain in the CDW phase, where alternating lattice displacements $\pm\Delta_i^{\mathrm{eq}}$ are accompanied by an alternating charge density n_i^{eq} varying around $1/2$. The indirect driving mechanism can be explained by looking at the potential energy profile of each lattice displacement, as illustrated in Fig. 1(b). The pump perturbs the equilibrium electronic order, thus changing the local charge density $n_i(t)$. The perturbed electronic state sets a new potential profile for the phonons at each site by rotating the equilibrium potential parabola around $\Delta_i = 0$ and setting a new dynamical minimum $\Delta_i^{\mathrm{min}}(t)$ [green dots in Fig. 1(b)] toward which each local displacement $\Delta_i(t)$ tends to move. For simulations starting at nonzero temperature, and in one dimension, there is no long-range order, so the order parameter represents the short-range order that governs the physics at low temperatures. This short-range order is stabilized in a finite-sized system, which is what we use for our calculations.

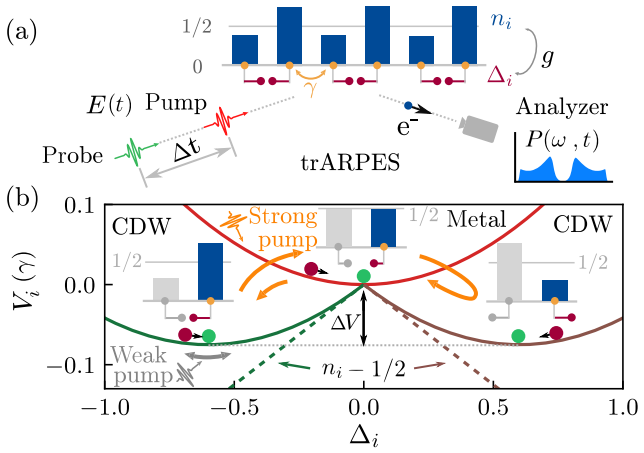

FIG. 1. (a) Schematics of the 1D Holstein chain of tight-binding sites (orange dots) with local lattice displacements Δ_i at every site (dark red dots and dark red lines below the orange dots) in our trARPES setup. A pump pulse $E(t)$ excites the electronic charge density n_i (dark blue bars) by modifying the Peierls phase factor of the tight-binding hopping parameter γ. The energy distribution of the injected electrons is captured in the computed photoemission spectrum $P(\omega, t)$. (b) Three potential energy profiles (green parabola, red parabola, and brown parabola) of a single lattice displacement Δ_i (dark red circles and dark red lines on the right side of the three insets above the parabolas) for different values of the on-site charge density n_i (blue bars on the right side of the three insets). Green dots show the potential minima of the three parabolas. The system is initialized at $T = 0$ temperature. The green and brown parabolas with green dots also show the two possible distorted charge-density-wave states with negative and positive displacements, respectively. For the context of what happens on the neighboring sublattice, see the grayed sites and bars on the left side of the three insets. The two possible distorted states are separated by an energy barrier ΔV. The pump excitation modifies the on-site charge density n_i, which rotates the potential energy parabola around the $\Delta_i = 0$ point (see the orange and gray arrows, which depict the motion of potential minima for strong and weak pump excitation, respectively). This happens because the derivative of the potential (9) at $\Delta_i = 0$ is $n_i - 1/2$ (the dashed green and brown lines). For uniform charge density, the system is considered to be metallic (inset above the red parabola), and the derivative is zero.

The pump can be considered strong or weak depending on its amplitude and frequency. Strong pumps drive the system from the initial CDW state in the left inset in Fig. 1(b) to an "overshot" state in the right inset with an inverted order parameter. The system left to itself after the pump oscillates between these two insulating CDW orders by briefly going through a metallic state [the top inset in Fig. 1(b)]. Flipping the CDW order, as exemplified by the site considered in Fig. 1(b), means the local charge density $n_i(t)$ goes below $1/2$ (if initially being above $1/2$), while the local displacement $\Delta_i(t)$ changes sign. By contrast, weak pumps only slightly perturb the initial CDW. They cause weak oscillations of the local displacements $\Delta_i(t)$ but never change their sign. We show both these scenarios, for the weak and the strong pump, in two videos in the Supplemental Material [45].

The pump-induced lattice motion changes the electronic structure of the system, causing the insulating gap energy to oscillate. The coupled dynamics repeat until the system reaches a new equilibrium. This behavior can be deduced from the computed PES intensity as well as from the order parameters for the electronic and lattice subsystems (see Sec. III A). In Sec. III B, we emphasize the differences between dynamics at $T = 0$ and at finite temperature. Additionally, we explore what the conditions are in terms of pump amplitude and frequency, which cause weak or strong driving (see Sec. III C). In the pumping regime that we consider, where the photon frequencies are at least one order of magnitude higher than the phonon ones, pump driving is modulated mostly by its amplitude. We find there is a threshold amplitude at which the driving begins and also another one which determines the transition from the weak to the strong pumping regime. We contrast this with a transient CDW melting regime

where the two subsystems are temporarily decoupled and the lattice freely oscillates at its intrinsic frequency. Additionally, we provide the details of electron dynamics and populations of the two subbands during the pump pulse in Sec. III D and in the Supplemental Material [45]. In Sec. III F, we show that our method can be used to simulate other experiments besides time-resolved PES, such as x-ray diffraction and 2D spectroscopy. Finally, we show in Sec. III G that our approach can be applied to higher-dimensional systems such as the 2D Holstein model.

II. OVERVIEW OF THE METHOD

The system illustrated in Fig. 1(a) is modeled by the 1D spinless Holstein model

$$\hat{H} = \hat{H}_{\rm el} + \hat{H}_{\rm ph}. \tag{1}$$

The electronic subsystem consists of a nearest-neighbor tight-binding model with uniform hopping γ and an electron-phonon interaction with coupling constant g, i.e.,

$$\hat{H}_{\rm el} = -\sum_{i=1}^{L}\left(\gamma \hat{c}_i^\dagger \hat{c}_{i+1} + \text{H.c.}\right) + g\sum_{i=1}^{L}\hat{q}_i\left(\hat{n}_i - \frac{1}{2}\right). \tag{2}$$

Here, $\hat{c}_i^\dagger$ and $\hat{c}_i$ are the electronic creation and annihilation operators, respectively, at lattice site i, while $\hat{q}_i$ is the local phonon displacement operator coupled to the local charge density $\hat{n}_i = \hat{c}_i^\dagger \hat{c}_i$. We impose periodic boundary conditions to eliminate edge effects. A time-varying pump field is implemented via the Peierls substitution $\gamma \to \gamma e^{-i\varphi(t)}$ on all sites, thus rendering the electronic Hamiltonian $\hat{H}_{\rm el}(t)$ explicitly time dependent. The hopping parameter γ sets the energy scale for our results, since we consider it as a basic unit of energy. To get a better connection with experiments where the energy is usually expressed in the units of eV, one can consider $\gamma = 1$ eV. Following Refs. [29,46], the probe is considered only perturbatively and is not included in the Peierls phase. Although in this paper we consider a spinless system, there is nothing in our method that prevents the inclusion of spin degrees of freedom.

The second term in the total Hamiltonian consists of the phonon kinetic and potential energy:

$$\hat{H}_{\rm ph} = \sum_{i=1}^{L}\frac{\hat{p}_i^2}{2M} + \sum_{i=1}^{L}\frac{K}{2}\hat{q}_i^2, \tag{3}$$

with K being the phonon spring constant and M the phonon mass; $\hat{p}_i$ is the phonon momentum operator. The electron-phonon interaction comes with a total of three parameters K, M, and g, but the physics of the model is fully determined by defining the following two ratios: the phonon frequency $\Omega = \sqrt{K/M}$ and the dimensionless electron-phonon coupling constant $\lambda = g^2/(4K\gamma)$. This can be seen by absorbing one of the three original couplings into the phonon coordinates (details are given below). Rescaling in this fashion holds even in the $M \to \infty$ limit, because of the rescaled coordinates, so we do not need to introduce a separate spring constant in that limit. This parametrization also becomes convenient when introducing the equations of motion below.

Throughout the remainder of the paper, we use γ as the unit of energy and set $\Omega = 0.01\gamma/\hbar$, $\lambda = 0.6$, and $L = 30$ (for the 1D case) if not stated otherwise. Because the approach described here derives from the static-phonon limit, it is most appropriate for systems with low renormalized phonon frequencies. This typically occurs in CDW systems, because a phonon often goes soft at the transition and then recovers at a low frequency in the ordered phase.

The Holstein model is one of the simplest models of electron-phonon coupling and is widely studied. If one wants to examine a more material-specific system, one can include an additional integration over the phonon frequency, weighted by the Eliashberg function $\alpha^2F(\Omega)$ in order to have a more material-specific calculation. We do not do that here; we simply point out that it can be incorporated if desired. It does require the assumption that the Eliashberg function does not get modified by the nonequilibrium excitation of the electrons, though. It also requires the material to be dirty enough that the anisotropic effects in the electron-phonon coupling are washed out due to disorder effects, so that only the energy dependence of the α^2F is relevant for the subsequent dynamics. This is essentially always true for conventional superconductors but may not be true for some CDW systems (if they have substantially smaller coherence lengths).

To solve for the long-time dynamics of the coupled electron-phonon system, we treat the electrons quantum mechanically but approximate the phonons by classical variables q_i and p_i. A classical description of the phonons becomes exact in the *frozen phonon* limit where $M \to \infty$ (i.e., $\Omega \to 0$). The quantum and classical harmonic oscillators are closely related to each other, especially if the harmonic oscillator has a large average energy. We state some of the facts about the quantum and classical oscillator that show this relationship. First, if the quantum state is described via a coherent state, then the time dependence of the average position and the momentum of the quantum oscillator are identical to that of a classical pulled mass on a spring. Second, if we compute the product of the fluctuations about the mean of the position and momentum over a period of oscillation for a classical harmonic oscillator, it is given by E/Ω, which is exactly what the quantum state uncertainty product is for energy eigenstates—the major difference is that the quantum oscillator has only an allowed set of energies. Third, if the average energy of the oscillator is larger than the phonon frequency, then the

difference between the quantum and classical expectation values become quite small and decreases as the average energy increases by Bohr's correspondence principle. The main difference is at low temperatures, because the classical oscillator can have energies smaller than $\frac{1}{2}\hbar\Omega$, and the fluctuations in position and momentum then both go to zero. This is clearly quite different from that of the quantum oscillator. Hence, in situations where the oscillator has a relatively large average energy, as compared to $\hbar\Omega$, the semiclassical approximation for the electron-phonon coupled problem is expected to be accurate. This should always occur when one pumps significant energy into a system to drive it to nonequilibrium, as we do in the work presented here. On the other hand, if the system is driven by a very weak pump so that it is very close to the equilibrium (and at very low temperature), the quantum phonon effects neglected by our approach do become important.

While the short-time response of the electrons to an applied pump field can be calculated efficiently in the static limit, the slow energy exchange between electrons and phonons requires small but finite phonon frequencies. To this end, we apply the Ehrenfest theorem to obtain the classical phonon equations of motion:

$$\frac{d}{dt}\Delta_i(t) = \Omega^2\pi_i(t), \tag{4}$$

$$\frac{d}{dt}\pi_i(t) = -\Delta_i(t) - 4\lambda\gamma(n_i(t) - 1/2), \tag{5}$$

for the rescaled classical variables $\Delta_i(t) = gq_i(t)$ and $\pi_i(t) = gp_i(t)/K$. Here, $n_i(t) = \langle\langle \hat{n}_i(t)\rangle\rangle_{\vec{\Delta}_0,\vec{\pi}_0}$ is the electronic expectation value of the charge density at time t, considering that the phonons were initialized in a configuration $(\vec{\Delta}_0, \vec{\pi}_0)$. The rhs in Eq. (5) defines a force that depends on the local phonon displacement $\Delta_i(t)$ and on the charge density $n_i(t)$.

For classical phonons, we calculate time-dependent observables

$$\langle\hat{O}(t)\rangle = \int d\vec{\Delta}_0 \int d\vec{\pi}_0 W_{\mathrm{eq}}(\vec{\Delta}_0, \vec{\pi}_0)\langle\langle\hat{O}(t)\rangle\rangle_{\vec{\Delta}_0,\vec{\pi}_0} \tag{6}$$

as a weighted average with respect to the equilibrium phonon distribution W_{eq}. We initialize our system in the equilibrium solution of the static phonon limit, which is accurate for temperatures $k_{\mathrm{B}}T \gtrsim \hbar\Omega$ [42]. Then, the initial phonon displacements $\vec{\Delta}_0$ are sampled from $W_{\mathrm{eq}}[\Omega = 0]$ using a classical MC method [47], and we set $\vec{\pi}_0 = 0$. At $T = 0$, our system is set up by a single configuration $\Delta_{0,i} = (-1)^i\Delta$ with perfect dimerization which is accompanied by CDW order, as illustrated in Fig. 1(a). A band gap of 2Δ separates the fully filled lower band from the empty upper band, so that the rescaled displacements are directly related to the single-particle gap Δ. Although there is no true long-range CDW order in 1D at $T > 0$, the band gap as well as short-range CDW correlations remain stable up to $k_{\mathrm{B}}T \approx 0.1\gamma$. For details on the equilibrium solution, see Ref. [47].

For each initial phonon configuration, the coupled electron-phonon dynamics is implemented self-consistently in two steps. In the first step, we update the electron annihilation operators $\hat{c}_i(t+\Delta t) = \sum_{j=1}^{L}\mathcal{U}_{ij}(t+\Delta t, t)\hat{c}_j(t)$ through evolution by direct diagonalization (for technical details, see Ref. [39]). This allows us to update $n_i(t)$. In the second step, the obtained $n_i(t)$ is replaced in Eq. (5) and new lattice displacements are computed using the Verlet integration scheme. Because $\hat{H}_{\mathrm{el}}(t)$ is quadratic for each phonon configuration, we need only $\mathcal{O}(L^3)$ operations for every time step (also because we do not consider any electron-electron interaction, for which matrix diagonalization would lead to an exponential scaling in L). This allows us to reach long enough times to observe the damped phonon oscillations also found in experiments. Note that the MC average over many initial phonon configurations recovers the interacting nature of our electron-phonon coupled system.

At $T = 0$, the perfectly dimerized state with $\Delta_{0,i} = (-1)^i\Delta$ remains a static (ground state) solution of the equations of motion if no field is applied, whereas our MC averaged quantities at $T > 0$ require a thermalization period ($20\,000\hbar/\gamma$ or approximately 20 ps) before we apply the pump. For all our simulations, we use a time step of $\Delta t = 0.1\hbar/\gamma$, which is set by the fast electron dynamics.

The chain is driven out of equilibrium with an external electric field applied uniformly in space along the x direction:

$$\mathbf{E}(\mathbf{r}, t) = E_0 \exp\left(-\frac{t^2}{2\sigma_{\mathrm{p}}^2}\right)\sin(\omega_{\mathrm{p}}t)\mathbf{e}_{\mathrm{x}}. \tag{7}$$

Here, E_0 is the pump amplitude, σ_{p} the pump width, ω_{p} the pump frequency, and $\mathbf{e}_{\mathrm{x}}$ the unit vector along the chain. The pump field modifies the phase $\varphi(t)$ of the nearest-neighbor hopping in Eq. (2) through the time-dependent vector potential $\mathbf{A}(\mathbf{r}, t) = -c\int^t \mathbf{E}(\mathbf{r}, t')dt'$; a spatially homogeneous field essentially shifts the electron momentum. We work in the gauge where the time-dependent scalar potential $\Phi(\mathbf{r}, t)$ is zero.

The time-dependent PES intensity is computed according to Ref. [46]:

$$P(\omega, t) = -i\int_{-\infty}^{\infty} dt_1 \int_{-\infty}^{\infty} dt_2 s(t_1 - t)s(t_2 - t)e^{-i\omega(t_1 - t_2)} \times \frac{1}{L}\sum_{i=1}^{L} G_{ii}^{<}(t_1, t_2), \tag{8}$$

where $G_{ii}^{<}(t_1, t_2) = i\langle\hat{c}_i^{\dagger}(t_2)\hat{c}_i(t_1)\rangle$ is the time-displaced local lesser Green's function and $s(t) = \exp[-t^2/2\sigma_{\mathrm{probe}}^2]/\sqrt{2\pi}\sigma_{\mathrm{probe}}$ is the shape of the probe pulse of width $\sigma_{\mathrm{probe}} =$

$10\hbar/\gamma$ centered at $t = 0$. This expression neglects matrix element effects for the photoemission process and is manifestly gauge invariant. We call it the PES intensity here, because we are neglecting matrix elements, which set the overall scale, so we can only compare to the experimental shape, that is the measured magnitude of the experimental results; experiments also use arbitrary units for the PES intensity.

III. RESULTS

A. Indirect driving mechanism and photoemission at a finite initial temperature

Insight on how the lattice is set in motion can be obtained from an effective phonon potential. By integrating the force in Eq. (5), we obtain a potential for a single lattice displacement:

$$V_i(\Delta_i) = \frac{1}{8\lambda\gamma}\Delta_i^2 + \Delta_i(n_i(t) - 1/2), \tag{9}$$

which is just the sum of the local phonon potential energy and the electron-phonon energy. For the perfectly dimerized chain, there are two possible ground states which differ from each other by the sign of Δ_i and $n_i - 1/2$ at every site [see the left and right insets in Fig. 1(b)]. When n_i changes, it rotates the potential parabola around $\Delta_i = 0$, because its steepness is given by the first derivative at that point, i.e., $n_i(t) - 1/2$. The equilibrium condition of the zero force at the potential minimum gives $\Delta_i^{\mathrm{eq}} = -4\lambda\gamma(n_i^{\mathrm{eq}} - 1/2)$ as well as the initial energy barrier $\Delta V = 2\lambda\gamma(n_i^{\mathrm{eq}} - 1/2)^2$ which separates the two ground states in Fig. 1(b). The equilibrium is perturbed by the pump, which modifies n_i^{eq} and sets a new dynamical minimum $\Delta_i^{\mathrm{min}}(t) = -4\lambda\gamma(n_i(t) - 1/2)$ [see the green dots in Fig. 1(b) and in the two Supplemental Material [45] videos] toward which $\Delta_i(t)$ starts to move. The pump is also modifying the initial energy barrier, making $\Delta V(t)$ time dependent. The barrier can completely disappear for $n_i(t) = 1/2$, allowing the lattice to transition from one excited ground state to another by flipping the sign of Δ_i.

As observed in experiments (see, e.g., Refs. [12,18]), the lattice motion causes the gap energy to oscillate, which is reflected in the computed PES intensity at low temperatures in Fig. 2. Both experimental and theoretical results do not depend strongly on dimensionality, as similar behavior is seen in 1D and 2D materials. The equilibrium spectrum before the pump is gapped (due to the Peierls distortion), which implies that only the lower band is populated. After excitation, the system will stabilize to a new equilibrium with a reduced gap energy. We call the state in the long-time limit (long after the pump pulse) the new equilibrium, because the system is expected to ultimately thermalize. Right after the pump, the system is considered to be in a nonequilibrium state. Since the pump added energy into the system and the system is closed, the temperature in the long-time limit will be higher than in the initial state.

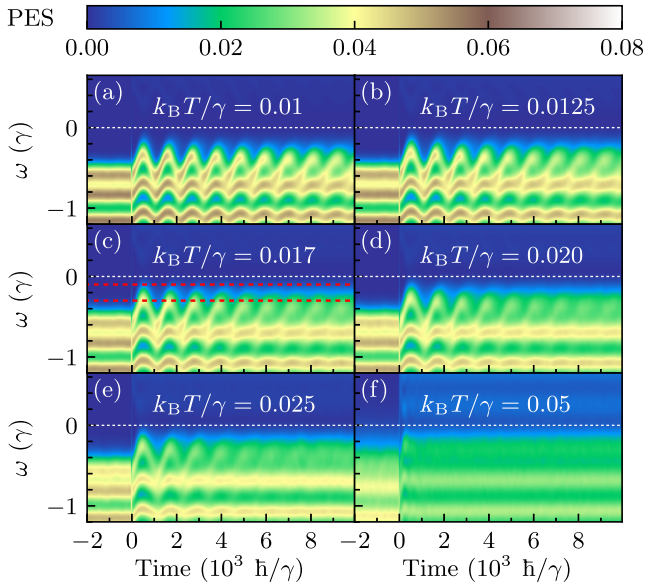

FIG. 2. Photoemission spectra intensity for a chain of $L = 30$ sites at different temperatures. The electron-phonon coupling is $\lambda = 0.6$, and the phonon frequency is $\Omega = 0.01\gamma/\hbar$. The pump parameters are $E_0 = 0.33$, $\sigma_{\mathrm{p}} = 10\hbar/\gamma$, and $\omega_{\mathrm{p}} = 0.1\gamma/\hbar$. The thin red dashed lines in (c) show the energy range where we average the PES intensity in order to compute the inverted intensity shown in Fig. 3(c). The finite size effects produce the "lumpiness" in these spectra, but the band edge behavior does not depend strongly on the lattice size, and that is the effect we focus on here.

Increasing the initial temperature of the lattice has two major effects on the computed PES intensity. The first is the evident damping of the gap oscillations, so the system relaxes faster to a new equilibrium PES for higher initial temperatures. The second effect is the "washing out" of the finer details in the spectrum at higher temperatures, increasing at longer times. The period of initial PES oscillations in Fig. 2(a) is much larger (around $1000\hbar/\gamma$) than what one would expect for $\Omega = 0.01\gamma/\hbar$, which is a clear sign that electron-phonon interaction significantly modifies the intrinsic phonon frequency. The advantage of our self-consistent MC approach is evident from the timescale of Fig. 2, where the time resolution must be kept at $0.1\hbar/\gamma$ to capture the electron dynamics; still, the fast evolution scheme allows us to average over 3000 MC configurations. Translating these units to the ones in experiments, for $\gamma = 1$ eV, the time step is $\Delta t \approx 0.07$ fs, while the simulation time is around 7 ps. For comparison, current time-dependent density-matrix renormalization group calculations have gone out only to the order of several femtoseconds (assuming a similar hopping energy of about 1 eV) [33–35].

The internal dynamics captured by the PES intensity in Fig. 2 is also reflected in two order parameters that track the behavior of the electronic and the lattice subsystem. For the electrons, we define the order parameter via the

time-dependent density-density correlation function at the ordering vector $q = \pi$:

$$S_{\mathrm{el}}(t) = \frac{1}{L}\sum_{j_1,j_2}(-1)^{j_1-j_2}\langle \hat{n}_{j_1}(t)\hat{n}_{j_2}(t)\rangle. \tag{10}$$

For the lattice, we define a similar correlation function of the local lattice displacements:

$$S_{\mathrm{ph}}(t) = \frac{1}{L}\sum_{j_1,j_2}(-1)^{j_1-j_2}\langle \Delta_{j_1}(t)\Delta_{j_2}(t)\rangle. \tag{11}$$

The oscillations of these two order parameters, shown in Figs. 3(a) and 3(b) for different temperatures, follow the average inverted PES intensity near the gap in Fig. 3(c). As with the PES intensity in Fig. 2, the order parameters are also stabilizing at a new equilibrium, with relaxation times inversely depending on the initial lattice temperature. For each initial temperature in Fig. 3(a), we fit the time dependence of $S_{\mathrm{el}}(t)$ with an exponentially decaying function $Ae^{-t/\tau}\cos(\omega_{\mathrm{f}}t)$ to determine the relevant relaxation time τ. The fitted decay times in Fig. 3(d) show that an initially hotter system relaxes faster toward the new equilibrium (at long times).

We observe similar relaxation dynamics for the electron and phonon energies in Fig. 3(f). During relaxation, the electrons exchange kinetic energy with the lattice, thus reducing the initial lattice displacement and thereby also the phonon potential energy $E_{\mathrm{ph}}^{\mathrm{pot}}$. The resulting oscillations in Fig. 3(f) are underdamped. The transfer of energy from electrons to phonons is a slow process, happening on a timescale significantly longer than those determined by relevant electronic and phonon energy scales. Because of the self-consistent nature of our method, we are able to predict these nontrivial timescales starting only from a tight-binding Hamiltonian in Eqs. (2) and (3) and without any additional assumptions about the given system. Note that the oscillating behavior can already be deduced from the zero-temperature results with a sliding time average, as shown in Fig. 3(e), but zero-temperature dynamics remains undamped and cannot give any insight into relaxation times.

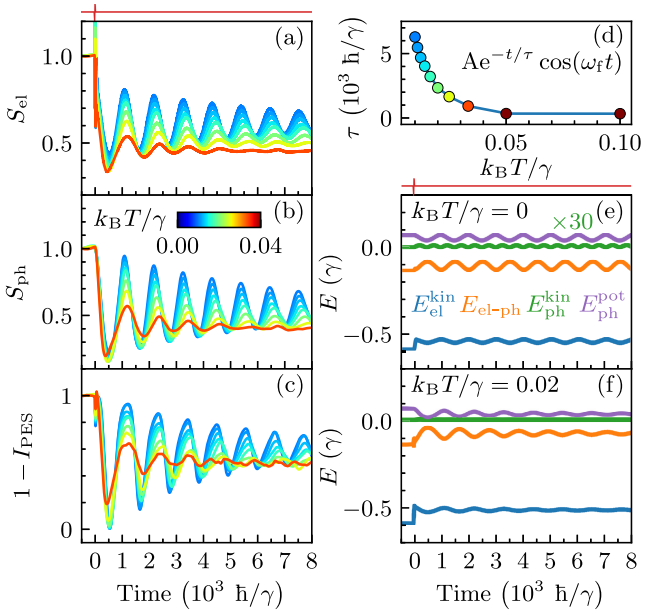

FIG. 3. (a), (b) Time evolution of the electron and phonon order parameters $S_{\mathrm{el}}(t)$ and $S_{\mathrm{ph}}(t)$, as defined in Eqs. (10) and (11), for different initial temperatures [see the color bar in (b)]. The order parameters are normalized to one before the pump is applied. (c) Time evolution of the inverse of a normalized in-gap PES intensity [averaged over the energy window between the two red lines in Fig. 2(c)] for the same temperatures as in (a) and (b). (d) Initial temperature dependence of the relaxation time τ extracted from (a) by fitting $S_{\mathrm{el}}(t)$ to the form $Ae^{-t/\tau}\cos(\omega_{\mathrm{f}}t)$; the relaxation time diverges as $T \to 0$. (e), (f) Time evolution of the energy expectation values per site of the different contributions in Eqs. (2) and (3), $E_{\mathrm{el}}^{\mathrm{kin}}$, $E_{\mathrm{el-ph}}$, $E_{\mathrm{ph}}^{\mathrm{kin}}$, and $E_{\mathrm{ph}}^{\mathrm{pot}}$, at temperatures $k_{\mathrm{B}}T = 0$ and $k_{\mathrm{B}}T = 0.02\gamma$. Because of the fast electron motion at $T = 0$ (due to no relaxation), the electronic energies in (e) are time averaged over 50 time steps (with a sliding time window). These time-averaged curves are similar to the nonzero initial T curves in (f) except they do not get damped. The time profile of the pump field is shown as a thin red curve above (a) and (e). The pump parameters are $\omega_{\mathrm{p}} = 0.1\gamma/\hbar$, $\sigma_{\mathrm{p}} = 10\hbar/\gamma$, and $E_0 = 0.33$, while for the phonons $\Omega = 0.01\gamma/\hbar$ and $\lambda = 0.6$.

B. Dynamics at the initial temperature of $T = 0$

As shown in Fig. 3(e), results at zero initial temperature are limited, because they do not show any damping effects, and once the system is excited it will continue to oscillate forever. On the other hand, computing the dynamics at $T = 0$ is numerically more efficient and requires far less computational resources, while it can be accurate in describing the dynamics during and right after the pump pulse, when damping effects are small (and we use a sliding time average). Figure 4 shows the raw data for the electron kinetic energy $E_{\mathrm{el}}^{\mathrm{kin}}$ and electron-phonon interaction $E_{\mathrm{el-ph}}$ and their

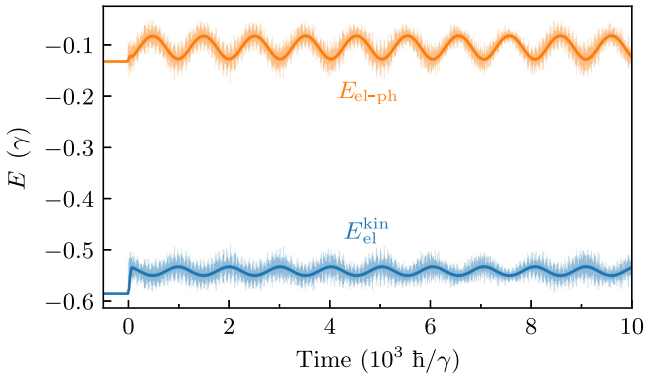

FIG. 4. Raw $T = 0$ results for the electron kinetic and potential energy (transparent background) and the corresponding time-averaged results (full color curves) presented in Fig. 3(e). The system parameters are $L = 30$, $\lambda = 0.6$, $\Omega = 0.01\gamma/\hbar$, $E_0 = 0.33$, $\omega_{\mathrm{p}} = 0.1\gamma/\hbar$, and $\sigma_{\mathrm{p}} = 10\hbar/\gamma$.

sliding time averages [also shown in Fig. 3(e)]. The electronic variables oscillate on two timescales. The smaller timescale is determined by the electron kinetic energy (fast oscillations on the order of a few $\hbar/\gamma$), while the larger timescale is determined by the phonon frequency (slow oscillations on the order of $10^3\hbar/\gamma$ obtained by the sliding time average). At a finite temperature, the fast electronic oscillations are smoothed out due to small phase differences between different MC configurations, while the slow oscillations caused by the phonons persist, at least for low temperatures. As shown in the next section, the dynamics at $T = 0$ temperature are very useful in determining different driving regimes the system exhibits when one increases the pump amplitude. Computing these regimes at a finite temperature is numerically very demanding, and currently it presents a challenge even for our Monte Carlo method.

Another advantage of the numerical efficiency of our method at zero temperature is that it allows one to perform simulations in large systems. Because of the time evolution through direct diagonalization combined with the sampling of many MC lattice configurations, the simulation time for a finite temperature increases drastically with the system size. Results obtained at $T = 0$, therefore, can provide an insight on how the dynamics changes with the system size, reaching sizes which are out of the scope of our MC method (starting at a finite temperature), but are also important in justifying our choice to perform simulations with $L = 30$ sites for $T > 0$. An example of this is shown in the photoemission spectrum at $T = 0$ in Fig. 5. The dynamics of the energy levels reveals the gap centered at $\omega = 0$, which is modulated by the symmetric motion of the upper and the lower band, a behavior previously observed experimentally [48]. Note that the discreteness of the spectra in the left part in Fig. 5 is due to the limited lattice size. We verify that $L = 30$ sites are sufficient to reliably estimate the oscillating gap (from the band edges) and that the PES intensity becomes continuous for $L = 100$, as shown in the right in Fig. 5. The numerical efficiency of simulating the dynamics at the zero temperature is used once again in the next section, where we check different pump driving regimes in systems consisting of $L = 600$ sites.

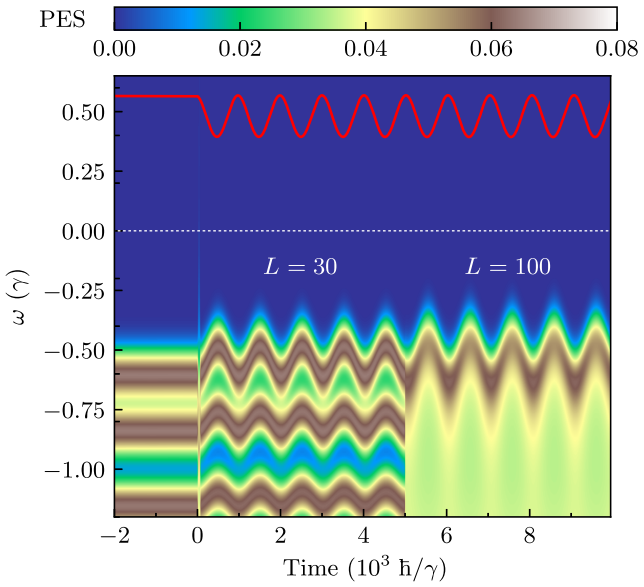

FIG. 5. The photoemission spectrum at $T = 0$ temperature. Data for times below $5 \times 10^3\hbar/\gamma$ are obtained for a system with $L = 30$ sites, while data above this time are obtained using a system with $L = 100$ sites. The red curve shows the oscillations of the phonon displacement, which corresponds to the gap energy $\Delta(t)$. Other parameters are the same as those used in Fig. 2: $\Omega = 0.01\gamma/\hbar$, $\lambda = 0.6$, $E_0 = 0.33$, $\sigma_p = 10\hbar/\gamma$, and $\omega_p = 0.1\gamma/\hbar$.

C. Driving regimes as a function of the pump amplitude

We examine the conditions for the weak and strong driving scenarios by modulating the square of the pump amplitude E_0^2 (which is proportional to its fluence) for the four pump pulse profiles in Fig. 6. For the first profile in Fig. 6(a), weak (strong) driving is illustrated in Fig. 6(e) for $E_0^2 = 0.1$ ($E_0^2 = 0.2$). The inversion of order at $E_0^2 = 0.2$ happens in both electronic and lattice subsystems simultaneously. To invert the order, the pump needs to exceed a threshold intensity [marked by the dashed yellow line in Fig. 6(i)]. The pump does not invert the order immediately, but it is the coupled dynamics of electrons and phonons which leads to the inversion only at later times [e.g., around $500\hbar/\gamma$ for $E_0^2 = 0.2$ in Fig. 6(e)], because the lattice moves much slower than the electrons. At the crossover intensity, the phonon amplitude saturates to a constant value [see the inset in Fig. 6(i)] and does not further change with E_0^2. This amplitude saturation as a function of fluence is one of the signatures of order inversion to look for in CDWs but also in other systems with degenerate ground states such as excitonic insulators, as recently demonstrated in Ref. [49].

We contrast the two driving regimes obtained from the pump in Fig. 6(a) with those obtained with pumps in Figs. 6(b)–6(d) with higher frequencies. In the melting regime, the electrons are almost instantly driven to a state with charge density oscillating around 1/2 [Figs. 6(f) and 6(g)]. The electron-phonon coupling at this point is effectively zero, and the electrons and phonons are dynamically decoupled for a period of time. This decoupling does not arise from g being renormalized to zero but rather from $n_i \approx \frac{1}{2}$, which makes the expectation value of the electron-phonon coupling small (even though the phonon still oscillates). In addition, the Ehrenfest force on the phonons becomes small for the same reason. Hence, in this case, phonons initially oscillate fully harmonically, as a sine

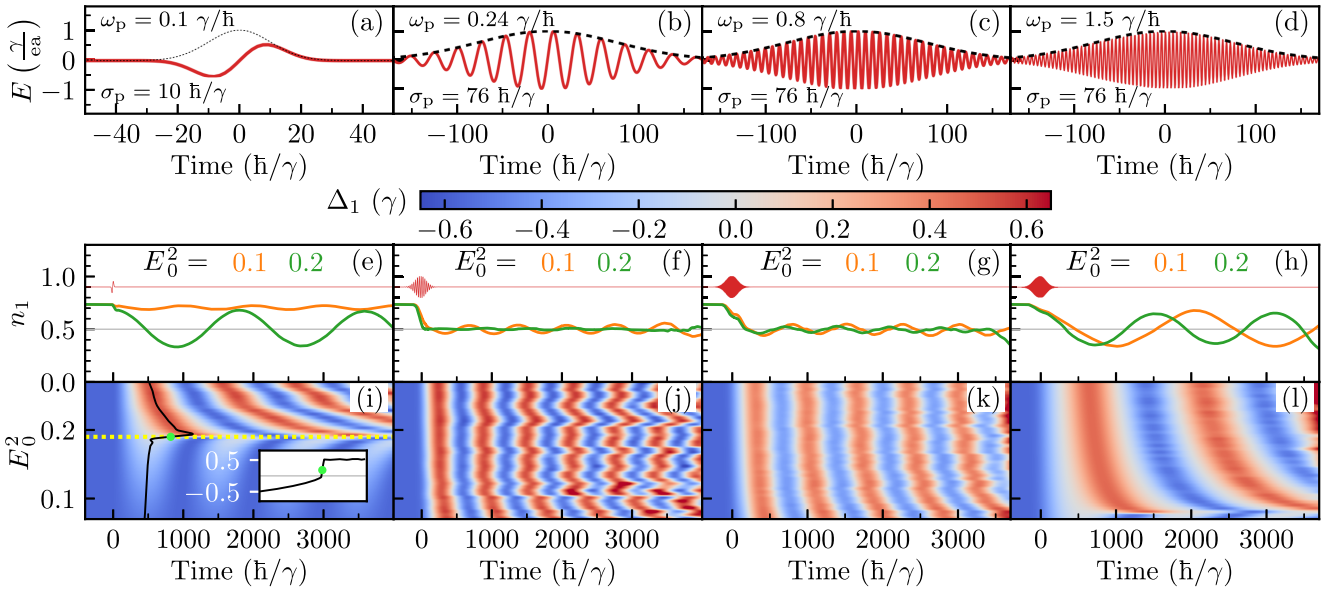

FIG. 6. Perturbation of CDW order for a system starting at $k_BT = 0$ by a pump. (a)–(d) Electric field (red curve) and its envelope function (dotted black curve) for four considered pump profiles. The pump used in Figs. 2 and 3 is presented in (a), while the pump with parameters set from Ref. [12] is in (d). In (b) and (c), we consider pumps with frequencies between the ones in (a) and (d). The field is given in units of $\gamma/(ea)$, where e is the electron charge and a is the lattice constant. (e)–(h) Time evolution of the charge density $n_1(t)$ on the first site of the chain for the pump profiles presented in the first row (a)–(d) and for two different amplitudes E_0^2. The thin red lines illustrate the time profiles of the four pulses from (a)–(d). The presented charge density is time averaged over a window of 50 time steps. (i)–(l) The time evolution of the phonon displacement $\Delta_1(t)$ on the first site of the lattice as a function of the pump intensity E_0^2 for the four pump profiles in (a)–(d), respectively. The dashed yellow line in (i) is the threshold intensity at which the lattice order changes sign. The inset in (i) tracks the amplitude of the first peak in Δ_1 as marked with the black curve in (i). The phonon frequency is $\Omega = 0.01\gamma/\hbar$, $\lambda = 0.6$, and $L = 600$.

wave with periodicity $2\pi/\Omega$ and a low amplitude [see Figs. 6(j) and 6(k)], just to be perturbed by the electrons at later times, once the electron-phonon coupling dynamically kicks in. The dependence on the pump intensity in Figs. 6(i)–6(l) is computed for $T = 0$. The results for low temperatures would be similar, because the damping effect caused by the temperature is low in the time range considered in Figs. 6(i)–6(l). Similar to the electronic energy in Fig. 3(e), the charge density at $T = 0$ is time averaged.

D. Band excitation during the pump pulse

The dispersion relation for our 1D CDW system consists of two bands separated by a gap Δ. The pump pulse excites the filled lower band and creates a nonequilibrium charge density by partially populating the upper band. In this section, we examine the details of this dynamics.

The first step in obtaining the populations of the two bands is to diagonalize the system Hamiltonian in k space. For $k_BT = 0$ and alternating phonon displacements $\Delta_i = (-1)^i\Delta$, the Hamiltonian in k space simplifies to

$$\hat{H}(k) = \sum_k \begin{pmatrix} \hat{c}_k^\dagger & \hat{c}_{k+\pi}^\dagger \end{pmatrix} \begin{pmatrix} \epsilon(k) & \Delta \\ \Delta & -\epsilon(k) \end{pmatrix} \begin{pmatrix} \hat{c}_k \\ \hat{c}_{k+\pi} \end{pmatrix}, \quad (12)$$

where $\epsilon(k) = -2\gamma\cos(k)$ is the 1D dispersion. The off-diagonal coupling between k and $k+\pi$ components reduces the Brillouin zone from $k \in [-(\pi/a), (\pi/a)]$ to $k \in [-(\pi/2a), (\pi/2a)]$. By diagonalizing the Hamiltonian in Eq. (12), one obtains the two bands $\epsilon^{\pm}(k) = \pm\sqrt{\epsilon(k)^2 + \Delta^2}$ [right inset in Fig. 7(b)]. The instantaneous diagonalization operators $\hat{X}_k$ allow for the computation of time-dependent creation and annihilation operators for the two bands in the reduced Brillouin zone (we drop the time label):

$$\begin{pmatrix} \hat{a}_{k+} \\ \hat{a}_{k-} \end{pmatrix} = \hat{X}_k \begin{pmatrix} \hat{c}_k \\ \hat{c}_{k+\pi} \end{pmatrix}, \quad (13)$$

which give the time-dependent population densities in the upper $n_k^+ = \langle \hat{a}_{k+}^\dagger \hat{a}_{k+} \rangle$ and the lower band $n_k^- = \langle \hat{a}_{k-}^\dagger \hat{a}_{k-} \rangle$.

Figure 7(b) shows the dynamics of the band excitation in k space during the pump pulse. Results are shifted in k so that the gap is now centered at $\pi/2a$. Initially, the system is excited around the gap where the energy difference between the two bands is minimal. As the vector potential increases, the excitations occur across the entire band, leading to a symmetric nonequilibrium distribution as the pump is switched off. There is no clear connection between the population of the two bands and the real space distribution of the charge density on the two sublattices [Fig. 7(c)].

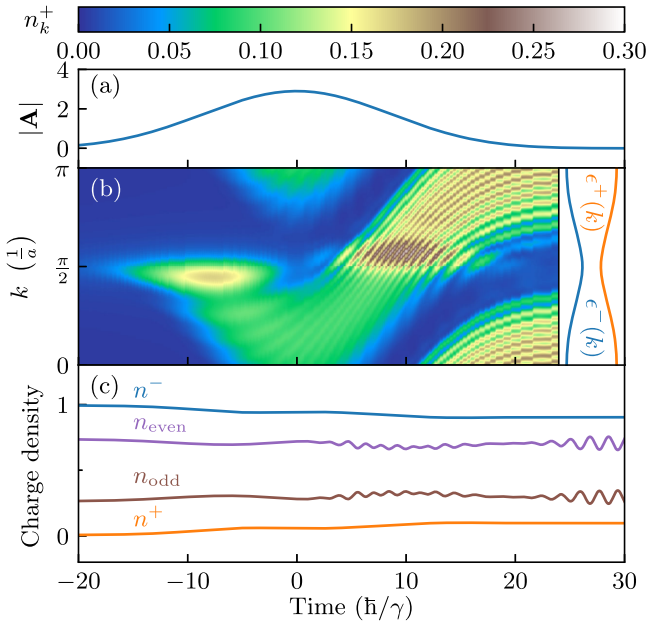

FIG. 7. Electron excitation dynamics in k space during the pump pulse at $k_B T = 0$. (a) Time evolution of the pump vector potential intensity. (b) Time evolution of the k-resolved occupation number for electrons in the upper band $n_k^+(t)$. The inset on the right shows the two bands $\epsilon^+(k)$ and $\epsilon^-(k)$ separated by a gap 2Δ for a 1D Holstein model. (c) Dynamics of the charge density in real space at odd and even sites $n_{\text{odd}}(t)$ and $n_{\text{even}}(t)$, respectively, compared to the populations of the upper $n^+(t)$ and the lower $n^-(t)$ bands in the reciprocal space. Populations $n^\pm(t)$ in each band are obtained by summing the k-resolved densities $n_k^\pm(t)$ in (b) over the reduced Brillouin zone. The system size is $L = 30$.

The population $n_k^- + n_k^+$ for each wave vector k is constant throughout time, so the two populations complement one another. The excitation (or deexcitation) is then always vertical (from n_k^- to n_k^+ and vice versa), and it involves changing the direction of the group velocity $\partial\epsilon/\partial k$. The initial excitation of $k > 0$ states for $t < 0$ leads to a finite current in the system and is followed by an excitation of the $k < 0$ states (equivalent to $k > \pi/2$) at later times. This can be understood semiclassically as follows: The initial rise of the vector potential corresponds to a force acting on the electrons and pushing them in one direction, only to be pushed in the opposite direction at later times (due to either Bragg diffraction or a change in the sign of the slope of the vector potential). The induced electronic state then creates the nonequilibrium potential for the phonons, setting the lattice into motion as described previously (but on a much longer timescale—one should think of the electrons as impulsively driving the phonons).

E. Comparison with other methods

As emphasized in the introduction, although our method uses the Ehrenfest theorem, it should not be confused with methods used in quantum chemistry such as MTE and FSSH. Similarly to our approach, both MTE and FSSH use classical lattice dynamics and independent trajectories sampled from an initial quantum phonon distribution. Here, we use a thermal (Boltzmann) distribution for the initial sampling and neglect quantum effects for the phonons. When it comes to computing the dynamics, although all three approaches (MTE, FSSH, and our method) rely on the split propagation scheme, where at each time step the electronic and lattice subsystems are updated self-consistently, the implementation details on how this is achieved (in particular, for the electrons) differ. An important difference is that our method does not rely on static potential energy surfaces and on a partially transformed Wigner density matrix. Instead, our method is based on nonequilibrium Greens functions often applied to solid-state systems. Computing the force in Eq. (5) using the expectation value of the charge density operator $n_i(t)$ makes our method more analogous to MTE, which is also a mean-field approach.

The exact diagonalization and basis transformation that we apply at every time step allows us to fully incorporate the time-dependent pump field into the system dynamics. This is not an easy task for MTE and FSSH. The pump field mixes the eigenenergy levels for every single MC trajectory even for the static lattice (Fig. 8). In the MTE and FSSH formalisms, these levels would represent a cross section of the potential-energy surfaces at the point $\mathbf{Q} = (q_1, q_2, q_3, \ldots, q_L)$ in the multidimensional phonon phase space. Because of the interaction with the field, the energy surfaces at this point would become dynamical, and they would change with the field even in the case of static phonons with $\Omega = 0$ (the situation becomes even more complicated when $\Omega \neq 0$). The crossing of energy levels during the pump pulse causes a mixing of the initial probability distributions associated with each potential energy surface, making it cumbersome to track

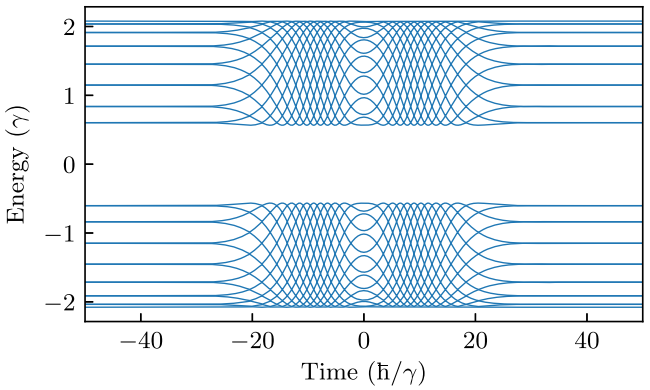

FIG. 8. Dynamics of the eigenenergy levels for a single static MC configuration ($\Omega = 0\gamma/\hbar$, $k_B T = 0.033\gamma$) during the pump pulse. The other parameters are $L = 30$ sites, $E_0 = 0.33$, $\sigma_p = 10\gamma/\hbar$, and $\omega_p = 0.1\gamma/\hbar$.

the electron trajectories in the presence of a field within the MTE and FSSH approaches. Since our method is based on exact diagonalization for the electronic system (which includes the time-dependent external field) and does not rely on static potential-energy surfaces, we find it more suitable for treating problems where the field is interacting with electron-phonon coupled systems. For the case considered in this paper, when the pump field is acting on timescales much smaller than the phonon period, the field perturbation of the initial probability distribution can be taken into consideration with MTE and FSSH by imposing new initial conditions after the pump pulse and assuming the phonon positions did not change significantly during the pump pulse. However, this becomes challenging for the case of resonant driving, when the field frequency matches that of the phonons in the lattice.

Another approach to describe the coupled electron-phonon dynamics is called generalized discrete truncated Wigner approximation (GDTWA) [50]. Similarly to MTE and FSSH, the GDTWA method is based on the sampling of independent trajectories from some initial phonon distribution in phase space. It differs from the two previous methods in the choice of the basis set used to expand the electronic operators, leading to different sampling of the initial electronic states and to a modified set of equations of motion. The method is very efficient when one deals with a small number of electronic states well separated in energy. The dynamics of the whole system then depends only on the few electronic states close to the ground state. The method is not suited to model electron-phonon dynamics in systems with large numbers of electronic states, which are energetically very close. In the case presented here, most states participate in the dynamics. This is commonly the situation for solid-state systems.

Lastly, the dynamics of electron-phonon coupled systems can be explored using time-dependent density functional theory (TDDFT) [51–55]. The advantage of TDDFT is that it provides a full microscopic description of the studied materials to a very high accuracy. Since our method is based on a tight-binding description, the results in our case are as good as the model parameters extracted from the first principles, and those can change with lattice motion, which might present problems when modeling real materials. TDDFT does not have this problem. On the other hand, the disadvantage of TDDFT is that (by default) it does not include the electron-phonon interaction in the system Hamiltonian and the Ehrenfest forces are introduced in an *ad hoc* way. Therefore, TDDFT does not accurately describe the process of energy exchange between the lattice and the electrons and has problems dealing with thermalization and decoherence [52]. Also, due to the high numerical demands, TDDFT can efficiently consider supercells of only a limited size and the dynamics on timescales significantly below the ones presented in this work.

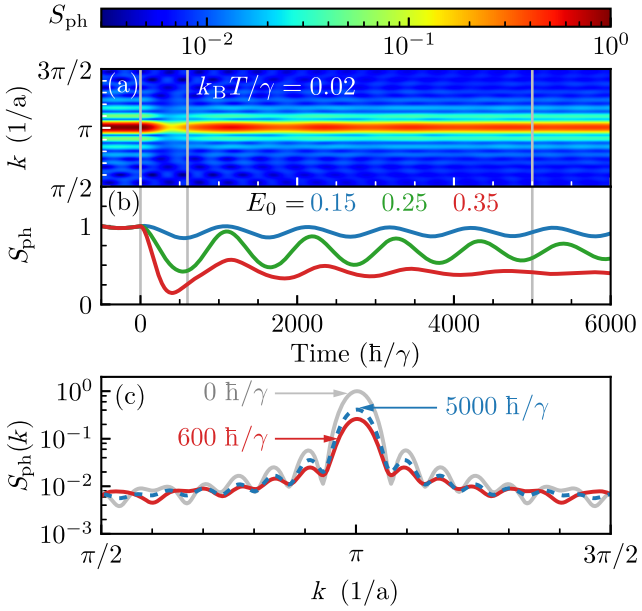

FIG. 9. X-ray diffraction in the 1D Holstein model. (a) Time dependence of the phonon structure factor $S_{\rm ph}(k)$ in k space. The initial temperature is $k_B T = 0.02\gamma$, and the pump amplitude is $E_0 = 0.35$. The structure factor is normalized by the value at $k = \pi$ at the zero time moment. (b) Time dependence of the structure factor at $k = \pi$ for different pump amplitudes. (c) Cross section of $S_{\rm ph}(k)$ from (a) for three different time steps [also marked in (a) and (b) by vertical lines]. There are $L = 30$ sites in the system, $\omega_{\rm p} = 0.1\gamma/\hbar$, $\Omega = 0.01\gamma/\hbar$, and $\sigma_p = 10\hbar/\gamma$.

F. X-ray diffraction and 2D spectroscopy

In previous sections, we focused on computing the photoemission spectrum measured in trPES experiments. However, our method is not limited to trPES and can be used to compute other observables, such as x-ray diffraction [21] (Fig. 9) or 2D spectroscopy (Fig. 10).

Because of the finite system size, the k-dependent structure factor in Fig. 9(a) shows periodic oscillations with changing k vector (these can be thought of as resonances due to the nearly periodic order in the sample). A similar effect has been observed experimentally [21] with x-ray diffraction on a CDW material. These wave-vector-dependent oscillations are already present in equilibrium, and they are further modified by the pump pulse. After the pump pulse at $t = 0$, all the peaks (including the main one at $k = \pi$) are suppressed and start to additionally oscillate in time. In Fig. 9(c), we show the cross section of the k-dependent structure factor for three different times: during the pump pulse (gray), during the first phonon oscillation (red), and in the long-time limit (blue). Although the main peak at $k = \pi$ and its neighboring peaks are suppressed by the pump, the k-dependent oscillations remain in the long-time limit with a small recovery. The pump-induced suppression of the structure factor is permanent (due to the addition of energy into the system, which ultimately

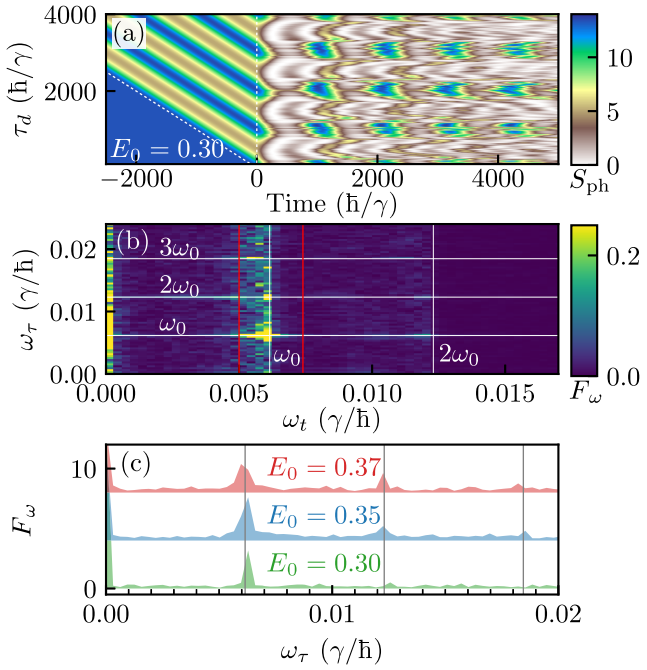

FIG. 10. 2D spectroscopy of the 1D Holstein model. (a) Time dependence of the phonon structure factor $S_{\rm ph}$ as a function of two-pump excitation. The positions of two pump pulses are marked by the two dashed lines. The two pumps are identical in amplitude, $E_0 = 0.3$, width $\sigma_p = 10\hbar/\gamma$, and frequency $\omega_{\rm p} = 0.1\gamma/\hbar$. (b) 2D spectroscopy map obtained by double Fourier transform of the data shown in (a). The main peak appears at (ω_0, ω_0) diagonal with $\omega_0 = 0.00615\gamma/\hbar$. (c) Sum of the Fourier coefficients F_ω in the range $0.005 < \omega_t < 0.0074$ [vertical red lines in (b)] showing off-diagonal components of the 2D spectrum. The data for different pump amplitudes are translated vertically to remove the overlap. There are $L = 100$ sites in the system, $\Omega = 0.01\gamma/\hbar$, and the initial temperature is zero.

heats it) as also shown by Fig. 9(b), where the structure factor is more suppressed for stronger pump amplitudes. Figure 9(b) additionally shows stronger damping of the oscillations for stronger pumps [compare the blue and red curves in Fig. 9(b)] and a fluence-dependent change in the oscillation frequency becoming a longer period for a higher fluence. This precise behavior has been observed experimentally in the oscillations of differential reflectivity in Refs. [56,57]. The modification of the oscillations of the structure factor, usually associated with a phonon frequency in the solid, arises from a nonlinear process, which can naively be thought of, in a first approximation, as arising from integrating out the electrons, which converts the linear electron-phonon coupling to a quadratic modification of the phonon frequency. But, because it also involves nonlinear effects, the precise nature of the modification is difficult to predetermine and needs to be numerically calculated, as we do here. The damping rate of these oscillations arises from a combination of both dynamic phonon disorder, which scatters electronic states, and electronic disorder, which is more prevalent at higher fluences, because they take us further away from a degenerate electron gas and cause more rapid dissipation of energy. To our knowledge, this is the first microscopic model that successfully predicts these two effects in time-resolved x-ray diffraction. We additionally fit the structure factor oscillations in Fig. 9(b) with exponentially decaying oscillatory functions. Lower fluences fit this form better than higher fluences. For more information, see the Supplemental Material [45], which quantitatively determines how the $S_{\rm ph}$ damping increases with increasing pump amplitude (accompanied by the increase in the oscillation period).

We also examine the so-called 2D spectroscopy [58–60], which is thought to be one of the next-generation probes to be used with newer x-ray free-electron lasers. In this experiment, two identical pump pulses are shot at the sample, with a time delay τ_d between them, and then they are followed by a probe pulse at an even further time delay. The additional pump is taken to be a copy of the first one but translated in time:

$$\mathbf{E}(\mathbf{r}, t, \tau_d) = E_0 \exp\left(-\frac{(t+\tau_d)^2}{2\sigma_{\rm p}^2}\right) \sin\left(\omega_{\rm p}(t+\tau_d)\right)\mathbf{e}_{\rm x}, \tag{14}$$

where τ_d is the time-translation constant. The first pump sets the lattice into motion at some (initial) negative time $(-\tau_d)$, and the second pump (centered at zero time) further excites the system (Fig. 10). One of the hallmarks of a two-dimensional experiment is that it promotes the excitation of multiple quanta due to a nonlinear process arising from the two pump pulses. By performing a double Fourier transform—one with respect to the time delay between the two pumps and one with respect to the time delay between the second pump and the probe—one obtains the so-called 2D spectrum, as shown in Fig. 10. What the spectrum illustrates is a very strongly pronounced peak along the diagonal (ω_0, ω_0). The response frequency ω_0 is smaller than the bare phonon frequency of Ω due to renormalization effects arising from the electron-phonon coupling (interaction with electrons slows down the phonon motion and renormalizes the phonon frequency). What is interesting is that besides the diagonal elements, which correspond to exciting single quanta, there is a significant excitation of the off-diagonal elements, particularly in the "vertical" direction around the ω_0 frequency. Smaller peaks at higher frequencies such as $2\omega_0$ and $3\omega_0$ can be seen in the 2D spectrum. While these are usually interpreted as multiquanta excitations, in our model, because we use semiclassical phonons, there is no multiquantum effect with phonon excitations. Instead, the $2\omega_0$ excitation can be interpreted along the lines of parametric excitation, as we discuss in more detail below. In general, the peak intensity depends on the strength of excitation by the pump pulse [Fig. 10(c)],

where stronger pumps induce higher peaks, especially off the main diagonal. One can think of the $2\omega_0$ excitation as similar to the process of pushing a child on a swing. Usually, we think of applying the pushes at the back of the child, every period. But we also can apply them at the front of the child, every half period, relative to the driving from the back. This then can excite a $2\omega_0$ response. Furthermore, depending on the timing and the direction of the push or pull, one can even enhance the amplitude of the swing when the push is not applied after a full period. This might also explain the $3\omega_0$ peak. Note that, for pump amplitudes higher than the ones considered in Fig. 10(c), the CDW order melts and there are no more regular oscillations of the lattice, so even the peak at the diagonal disappears.

To get a better understanding of the vertical (off-diagonal) peaks in the 2D spectrum, in Fig. 11(a) we show the sum of Fourier amplitudes around the main peak ω_0 but without performing the second Fourier transform (the one with respect to pump-pump delay). Further transforming these data, one would obtain the off-diagonal peaks in Fig. 10(a). The data in Fig. 11(a) are not a simple sine wave and cannot be associated with a single oscillation frequency. This further indicates the strong nonlinear response of the system. In addition, we have an interesting correlation between the 2D spectroscopy and dynamical slowing down [61]. The two sharp dips (just below 1000 time steps and near 2000 time steps) occur because the system has dynamical slowing down and can even be used to identify precisely where dynamical slowing down occurs, so it can be further studied (this can be particularly useful experimentally). This can be seen in more detail in Fig. 11(d), which is focused at the dip near 2000 time steps.

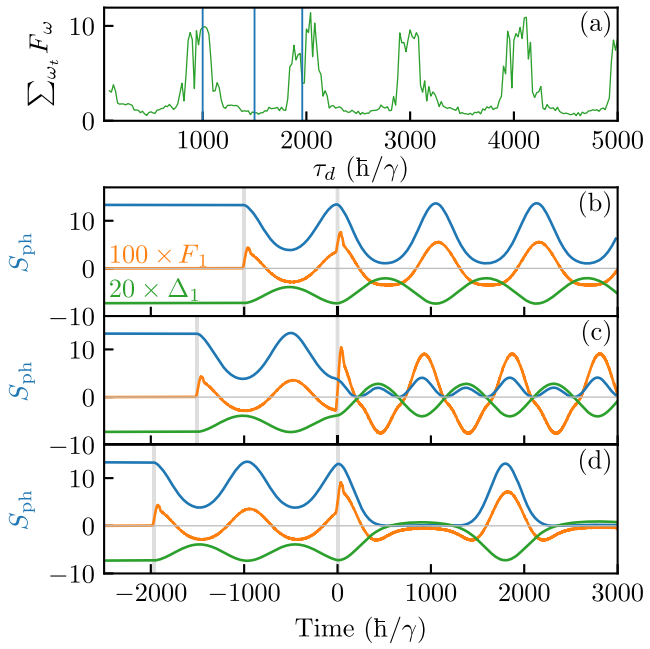

FIG. 11. (a) Sum of the Fourier amplitudes F_ω in the range $\omega_t \in (0.005, 0.007)\gamma/\hbar$ for different two-pump delays τ_d. Time dependence of the phonon structure factor $S_{\rm ph}$ (blue curve) for different delays of the second pump (b) $\tau_d = 1000\hbar/\gamma$, (c) $\tau_d = 1500\hbar/\gamma$, and (d) $\tau_d = 1965\hbar/\gamma$. The orange curve shows the scaled force F_1 acting on the first site, while the green curve shows the scaled first phonon coordinate Δ_1. The vertical gray areas mark the time periods when two pumps are active. All parameters are the same as in Fig. 10.

G. 2D Holstein model

The results we have presented have been limited to the 1D Holstein model, but the methodology can be applied to higher-dimensional systems at a greatly expanded computational cost. To illustrate this, we apply our method to a 2D Holstein sheet of 20×20 lattice sites with the periodic boundary conditions. The system that we consider is initially at zero temperature and similar to the 1D system has two possible ground states which differ just by a sign of the

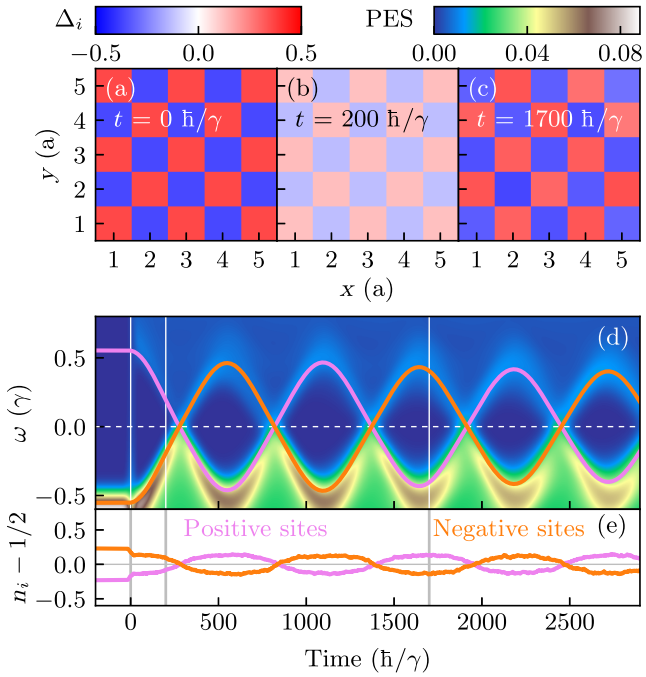

FIG. 12. CDW oscillations in a 2D Holstein model. (a)–(c) Phonon coordinates Δ_i of a 5×5 piece of the 2D Holstein sheet ($L_x = 20 \times L_y = 20$) at different time moments showing CDW inversion in (c). (d) Photoemission spectrum of the 2D Holstein sheet. The violet curve shows the average phonon coordinate obtained from all positive sites [red sites in (a)], while the orange curve shows the average phonon coordinate for all negative sites [blue sites in (a)]. (e) Average on-site charge density for all positive and negative sites of the 2D Holstein sheet. The vertical lines in (d) and (e) mark the three time moments for which we show the phonon coordinates in (a)–(c). The coupling constant is $\lambda = 0.6$, the phonon frequency is $\Omega = 0.01\hbar/\gamma$, the pump amplitude is $E_{0x} = E_{0y} = 0.5$, with $\sigma_p = 10\hbar/\gamma$ and $\omega_p = 0.1\gamma/\hbar$, and the probe parameters are the same as in the 1D case. The temperature is zero.

phonon coordinates. We pick one of the two states [shown in Fig. 12(a)] as the initial state. The pump pulse is chosen to lie along the diagonal direction, so it has two components: one along the x direction and one along the y direction. We use the same pump profile along the y as the one along the x and given by Eq. (7). A sufficiently strong pump causes an inversion of the CDW order, as shown in Fig. 12(c). The inversion of the phonon coordinates in Fig. 12(c) is accompanied by an inversion of the on-site charge density, as shown in Fig. 12(e). The photoemission spectrum also illustrates characteristic signatures of the CDW inversion. Compared to Fig. 5, where the pump causes just a modulation of the gap energy in the form of a sine wave, we find in Fig. 12(d) that the gap is closed at certain instants in time at the intersections of two sine waves.

Our results on the 2D system are just a short preview of how our method can be applied in higher dimensions. A systematic study as a function of the initial temperature will illustrate many more properties of these systems. We leave this to future work due to the significant computational cost required for such work.

IV. DISCUSSION

We demonstrated that our time-dependent semiclassical MC modeling captures the experimentally observed dynamics of electron-phonon coupled systems driven out of equilibrium, starting from the initial excitation to the subsequent relaxation at finite temperatures. This is made possible because we preserve the quantum-mechanical behavior of the electrons, but we treat the phonons semiclassically using Ehrenfest forces from the electrons. We use a small time step on the electronic timescale but accumulate the result to much longer timescales relevant for the phonons. This approach now allows many recent (and future) ultrafast experiments to be analyzed microscopically rather than phenomenologically.

In this work, we have concentrated on an indirect driving mechanism for the lattice dynamics, where the excited electrons "impulse" the phonons, and the phonon motion extends over much longer timescales. In future studies, a direct coupling of the lattice to the field may give additional insight into the interplay between indirect and direct driving mechanisms. Moreover, different types of electron-phonon interaction can lead to a periodic lattice distortion accompanied by charge order, which opens up new questions about their pump-probe dynamics. For example, in the Su-Schrieffer-Heeger model [62], the diagonal coupling of lattice displacements and on-site charge density is replaced with an off-diagonal coupling between deviations of neighboring bond length and the neighboring hopping. However, the equations of motion remain of the same form; therefore, the indirect driving mechanism revolves around the pump driving a local bond current, which modifies the local bond length. Another question is how the indirect driving mechanism is influenced by anharmonic potential terms like $\sum_i \Omega_4 \Delta_i^4$ considered in Ref. [63]. Although this term modifies the shape of the potential energy curve for each lattice displacement, a connection between the time-dependent charge density $n_i(t)$ and the local displacement minima still exists.

A nonlinear coupling of the electronic density to the phonon coordinates, as studied for equilibrium systems in Ref. [64], can be included as well and might be important at large field strengths. In addition, we have demonstrated that, with additional computational cost, our approach can be extended to two dimensions [39], but we leave an extensive study of the two-dimensional systems for future studies.

It is comforting to know that our explanation of the indirect driving in terms of the modification of the local lattice potential and the reduction of the energy barrier is very similar to the standard phenomenological Ginzburg-Landau (GL) model, often employed to explain pump-probe experiments in CDW materials. The GL model predicts a double-well structure in the free-energy potential, which upon excitation with a strong pump can turn into a single-well potential where the order parameter oscillates around zero [14]. Here, we propose an efficient complementary approach to GL, which allows for a more detailed microscopic exploration with consideration of the full Hamiltonian of the system but without the computational cost of a more demanding first-principles method such as, for example, TDDFT. We view our method as a balanced alternative, which offers a way to self-consistently induce lattice motion by direct coupling with the pump field and to evolve the system to timescales relevant for phonon effects to appear. The damping of the phonon oscillations emerges naturally from our finite-temperature method, without the need to modify the lattice equations of motion in order to include damping in a phenomenological way. Another important characteristic of our time evolution scheme is that it includes the electronic degrees of freedom and it produces a true nonequilibrium electronic state, without any additional assumptions regarding the timescales it takes for electrons to thermalize. This opens up the possibility to examine many different types of pump-probe experiments.

The inversion of the lattice order, accompanied by the inversion of electronic charge density ordering, is not a specific feature of just CDW systems. A similar mechanism was recently reported and measured in excitonic insulators [49]. A double pump pulse was used to modulate the phonon oscillations and suppress or enhance the phonon amplitude, and the enhancement was related to the inverted structural order. A similar modulation of the phonon amplitude was also reported for tritellurides [48], although it was not directly associated with the inversion of order. The possibility to invert the order appears to be a general feature of all systems with degenerate ground states

coupled to the lattice. An interesting feature of the order inversion brought out by our theoretical work is that a system can briefly pass through a metastable state where electrons and phonons are effectively decoupled, so the inversion of order is accompanied with a state that might have dramatically different conductivity (because the Holstein-like electron-phonon coupling vanishes when the phonon coordinate lies at the origin). It will be exciting to apply our methodology to these interesting problems.

We want to end with a cautionary note. While we have been able to show that results from these calculations display a number of different experimentally seen phenomena, we have not been able to independently benchmark these results against other known accurate methods such as exact diagonalization or density-matrix renormalization group calculations. This is because our results are anticipated to be most accurate in regimes that are not so readily accessible to these alternative methods. We hope that, in the future, it will be possible to benchmark this approach against alternative methods to better understand fully its overall accuracy.

ACKNOWLEDGMENTS

This work was supported by the U.S. Department of Energy, Office of Science, Basic Energy Sciences under Grant No. DE-FG02-08ER46542. J. K. F. was also supported by the McDevitt bequest at Georgetown University. We acknowledge our discussions with Keith Nelson on the subject of 2D spectroscopy and with Samuel Teitelbaum, who pointed out the experimental relevance of the change in the damping rate and oscillation frequency with the pump fluence in Fig. 9(b). This research used resources of the National Energy Research Scientific Computing Center, a U.S. Department of Energy Office of Science User Facility operated under Contract No. DE-AC02-05CH11231. This work was supported by the Deutsche Forschungsgemeinschaft through the Würzburg-Dresden Cluster of Excellence on Complexity and Topology in Quantum Matter—ct.qmat (EXC 2147, Project No. 390858490).

[1] S. Hellmann, C. Sohrt, M. Beye, T. Rohwer, F. Sorgenfrei, M. Marczynski-Bühlow, M. Kalläne, H. Redlin, F. Hennies, M. Bauer, A. Föhlisch, L. Kipp, W. Wurth, and K. Rossnagel, *Time-resolved x-ray photoelectron spectroscopy at FLASH*, New J. Phys. **14**, 013062 (2012).

[2] M. Na, A. K. Mills, and D. J. Jones, *Advancing time- and angle-resolved photoemission spectroscopy: The role of ultrafast laser development*, Phys. Rep. **1036**, 1 (2023).

[3] F. Boschini, M. Zonno, and A. Damascelli, *Time-resolved ARPES studies of quantum materials*, Rev. Mod. Phys. **96**, 015003 (2024).

[4] J. A. Sobota, Y. He, and Z.-X. Shen, *Angle-resolved photoemission studies of quantum materials*, Rev. Mod. Phys. **93**, 025006 (2021).

[5] S. Gerber *et al.*, *Femtosecond electron-phonon lock-in by photoemission and x-ray free-electron laser*, Science **357**, 71 (2017).

[6] S. Aeschlimann, S. A. Sato, R. Krause, M. Chávez-Cervantes, U. De Giovannini, H. Hübener, S. Forti, C. Coletti, K. Hanff, K. Rossnagel, A. Rubio, and I. Gierz, *Survival of Floquet–Bloch states in the presence of scattering*, Nano Lett. **21**, 5028 (2021).

[7] J. A. Sobota, S. Yang, J. G. Analytis, Y. L. Chen, I. R. Fisher, P. S. Kirchmann, and Z.-X. Shen, *Ultrafast optical excitation of a persistent surface-state population in the topological insulator* Bi_2Se_3, Phys. Rev. Lett. **108**, 117403 (2012).

[8] G. Gruner, *Density Waves in Solids* (Taylor & Francis, London, 1994).

[9] G. Grüner, *The dynamics of charge-density waves*, Rev. Mod. Phys. **60**, 1129 (1988).

[10] L. Perfetti, P. A. Loukakos, M. Lisowski, U. Bovensiepen, H. Berger, S. Biermann, P. S. Cornaglia, A. Georges, and M. Wolf, *Time evolution of the electronic structure of* $1T-TaS_2$ *through the insulator-metal transition*, Phys. Rev. Lett. **97**, 067402 (2006).

[11] L. Perfetti, P. A. Loukakos, M. Lisowski, U. Bovensiepen, M. Wolf, H. Berger, S. Biermann, and A. Georges, *Femtosecond dynamics of electronic states in the Mott insulator* $\times 1T\text{-}TaS_2$ *by time resolved photoelectron spectroscopy*, New J. Phys. **10**, 053019 (2008).

[12] F. Schmitt, P. S. Kirchmann, U. Bovensiepen, R. G. Moore, L. Rettig, M. Krenz, J.-H. Chu, N. Ru, L. Perfetti, D. H. Lu, M. Wolf, I. R. Fisher, and Z.-X. Shen, *Transient electronic structure and melting of a charge density wave in* $TbTe_3$, Science **321**, 1649 (2008).

[13] F. Schmitt, P. S. Kirchmann, U. Bovensiepen, R. G. Moore, J.-H. Chu, D. H. Lu, L. Rettig, M. Wolf, I. R. Fisher, and Z.-X. Shen, *Ultrafast electron dynamics in the charge density wave material* $TbTe_3$, New J. Phys. **13**, 063022 (2011).

[14] J. Maklar, Y. W. Windsor, C. W. Nicholson, M. Puppin, P. Walmsley, V. Esposito, M. Porer, J. Rittmann, D. Leuenberger, M. Kubli, M. Savoini, E. Abreu, S. L. Johnson, P. Beaud, G. Ingold, U. Staub, I. R. Fisher, R. Ernstorfer, M. Wolf, and L. Rettig, *Nonequilibrium charge-density-wave order beyond the thermal limit*, Nat. Commun. **12**, 2499 (2021).

[15] A. Kogar *et al.*, *Light-induced charge density wave in* $LaTe_3$, Nat. Phys. **16**, 159 (2020).

[16] A. Zong, P. E. Dolgirev, A. Kogar, Y. Su, X. Shen, J. A. W. Straquadine, X. Wang, D. Luo, M. E. Kozina, A. H. Reid, R. Li, J. Yang, S. P. Weathersby, S. Park, E. J. Sie, P. Jarillo-Herrero, I. R. Fisher, X. Wang, E. Demler, and N. Gedik, *Role of equilibrium fluctuations in light-induced order*, Phys. Rev. Lett. **127**, 227401 (2021).

[17] M. Chollet, L. Guerin, N. Uchida, S. Fukaya, H. Shimoda, T. Ishikawa, K. Matsuda, T. Hasegawa, A. Ota, H. Yamochi, G. Saito, R. Tazaki, S. ichi Adachi, and S. ya Koshihara, *Gigantic photoresponse in ¼-filled-band organic salt* $(EDO\text{-}TTF)_2PF_6$, Science **307**, 86 (2005).

[18] H. Y. Liu, I. Gierz, J. C. Petersen, S. Kaiser, A. Simoncig, A. L. Cavalieri, C. Cacho, I. C. E. Turcu, E. Springate, F. Frassetto, L. Poletto, S. S. Dhesi, Z.-A. Xu, T. Cuk, R. Merlin, and A. Cavalleri, *Possible observation of parametrically amplified coherent phasons in* $K_{0.3}MoO_3$ *using time-resolved extreme-ultraviolet angle-resolved photoemission spectroscopy*, Phys. Rev. B **88**, 045104 (2013).

[19] H. Hübener, U. De Giovannini, and A. Rubio, *Phonon driven floquet matter*, Nano Lett. **18**, 1535 (2018).

[20] A. Zong, A. Kogar, and N. Gedik, *Unconventional light-induced states visualized by ultrafast electron diffraction and microscopy*, MRS Bull. **46**, 720 (2021).

[21] A. Singer, S. K. K. Patel, R. Kukreja, V. Uhlíř, J. Wingert, S. Festersen, D. Zhu, J. M. Glownia, H. T. Lemke, S. Nelson, M. Kozina, K. Rossnagel, M. Bauer, B. M. Murphy, O. M. Magnussen, E. E. Fullerton, and O. G. Shpyrko, *Photoinduced enhancement of the charge density wave amplitude*, Phys. Rev. Lett. **117**, 056401 (2016).

[22] A. Zong, A. Kogar, Y.-Q. Bie, T. Rohwer, C. Lee, E. Baldini, E. Ergeçen, M. B. Yilmaz, B. Freelon, E. J. Sie, H. Zhou, J. Straquadine, P. Walmsley, P. E. Dolgirev, A. V. Rozhkov, I. R. Fisher, P. Jarillo-Herrero, B. V. Fine, and N. Gedik, *Evidence for topological defects in a photoinduced phase transition*, Nat. Phys. **15**, 27 (2019).

[23] F. Zhou, J. Williams, S. Sun, C. D. Malliakas, M. G. Kanatzidis, A. F. Kemper, and C.-Y. Ruan, *Nonequilibrium dynamics of spontaneous symmetry breaking into a hidden state of charge-density wave*, Nat. Commun. **12**, 566 (2021).

[24] I. Gonzalez-Vallejo, V. L. R. Jacques, D. Boschetto, G. Rizza, A. Hadj-Azzem, J. Faure, and D. Le Bolloc'h, *Time-resolved structural dynamics of the out-of-equilibrium charge density wave phase transition in* $GdTe_3$, Struct. Dyn. **9**, 014502 (2022).

[25] S. Vogelgesang, G. Storeck, J. G. Horstmann, T. Diekmann, M. Sivis, S. Schramm, K. Rossnagel, S. Schäfer, and C. Ropers, *Phase ordering of charge density waves traced by ultrafast low-energy electron diffraction*, Nat. Phys. **14**, 184 (2018).

[26] B. Moritz, T. P. Devereaux, and J. K. Freericks, *Time-resolved photoemission of correlated electrons driven out of equilibrium*, Phys. Rev. B **81**, 165112 (2010).

[27] O. P. Matveev, A. M. Shvaika, T. P. Devereaux, and J. K. Freericks, *Time-domain pumping a quantum-critical charge density wave ordered material*, Phys. Rev. B **94**, 115167 (2016).

[28] W. Shen, T. P. Devereaux, and J. K. Freericks, *Beyond Planck-Einstein quanta: Amplitude-driven quantum excitation*, Phys. Rev. B **90**, 195104 (2014).

[29] W. Shen, Y. Ge, A. Y. Liu, H. R. Krishnamurthy, T. P. Devereaux, and J. K. Freericks, *Nonequilibrium "melting" of a charge density wave insulator via an ultrafast laser pulse*, Phys. Rev. Lett. **112**, 176404 (2014).

[30] J. K. Freericks, O. P. Matveev, W. Shen, A. M. Shvaika, and T. P. Devereaux, *Theoretical description of pump/probe experiments in electron-mediated charge-density-wave insulators*, Phys. Scr. **92**, 034007 (2017).

[31] P. Werner and M. Eckstein, *Nonequilibrium resonant inelastic x-ray scattering study of an electron-phonon model*, Phys. Rev. B **104**, 085155 (2021).

[32] G. De Filippis, V. Cataudella, E. A. Nowadnick, T. P. Devereaux, A. S. Mishchenko, and N. Nagaosa, *Quantum dynamics of the Hubbard-Holstein model in equilibrium and nonequilibrium: Application to pump-probe phenomena*, Phys. Rev. Lett. **109**, 176402 (2012).

[33] H. Matsueda, S. Sota, T. Tohyama, and S. Maekawa, *Relaxation dynamics of photocarriers in one-dimensional mott insulators coupled to phonons*, J. Phys. Soc. Jpn. **81**, 013701 (2012).

[34] H. Hashimoto and S. Ishihara, *Photoinduced charge-order melting dynamics in a one-dimensional interacting Holstein model*, Phys. Rev. B **96**, 035154 (2017).

[35] J. Stolpp, J. Herbrych, F. Dorfner, E. Dagotto, and F. Heidrich-Meisner, *Charge-density-wave melting in the one-dimensional Holstein model*, Phys. Rev. B **101**, 035134 (2020).

[36] C. Brockt, F. Dorfner, L. Vidmar, F. Heidrich-Meisner, and E. Jeckelmann, *Matrix-product-state method with a dynamical local basis optimization for bosonic systems out of equilibrium*, Phys. Rev. B **92**, 241106(R) (2015).

[37] J. Sous, B. Kloss, D. M. Kennes, D. R. Reichman, and A. J. Millis, *Phonon-induced disorder in dynamics of optically pumped metals from nonlinear electron-phonon coupling*, Nat. Commun. **12**, 5803 (2021).

[38] H. J. Zeiger, J. Vidal, T. K. Cheng, E. P. Ippen, G. Dresselhaus, and M. S. Dresselhaus, *Theory for displacive excitation of coherent phonons*, Phys. Rev. B **45**, 768 (1992).

[39] M. Weber and J. K. Freericks, *Real-time evolution of static electron-phonon models in time-dependent electric fields*, Phys. Rev. E **105**, 025301 (2022).

[40] R. Car and M. Parrinello, *Unified approach for molecular dynamics and density-functional theory*, Phys. Rev. Lett. **55**, 2471 (1985).

[41] S. A. Brazovskii and I. E. Dzyaloshinskii, *Dynamics of one-dimensional electron-phonon systems at low temperatures*, Zh. Eksp. Teor. Fiz. **71**, 2338 (1976).[Sov. Phys. JETP **44**, 1233 (1976)], http://www.jetp.ras.ru/cgi-bin/e/index/e/44/6/p1233?a=list.

[42] M. Weber, F. F. Assaad, and M. Hohenadler, *Thermal and quantum lattice fluctuations in Peierls chains*, Phys. Rev. B **98**, 235117 (2018).

[43] R. Crespo-Otero and M. Barbatti, *Recent advances and perspectives on nonadiabatic mixed quantum–classical dynamics*, Chem. Rev. **118**, 7026 (2018).

[44] M. ten Brink, S. Gräber, M. Hopjan, D. Jansen, J. Stolpp, F. Heidrich-Meisner, and P. E. Blöchl, *Real-time non-adiabatic dynamics in the one-dimensional Holstein model: Trajectory-based vs exact methods*, J. Chem. Phys. **156**, 234109 (2022).

[45] See Supplemental Material at http://link.aps.org/supplemental/10.1103/PhysRevX.14.031052 for videos of the CDW dynamics at zero temperature for a weak and a strong pump pulse and a video showing dynamics in k space like in Fig. 7. The Supplemental Material additionally provides more information on the oscillations of the phonon structure factor in Fig. 9(b) in the main text, namely the fluence-dependent change in the oscillation decay and the oscillation period.

[46] J. K. Freericks, H. R. Krishnamurthy, and T. Pruschke, *Theoretical description of time-resolved photoemission spectroscopy: Application to pump-probe experiments*, Phys. Rev. Lett. **102**, 136401 (2009).

[47] M. Weber, F. F. Assaad, and M. Hohenadler, *Thermodynamic and spectral properties of adiabatic Peierls chains*, Phys. Rev. B **94**, 155150 (2016).

[48] L. Rettig, J.-H. Chu, I. R. Fisher, U. Bovensiepen, and M. Wolf, *Coherent dynamics of the charge density wave gap in tritellurides*, Faraday Discuss. **171**, 299 (2014).

[49] H. Ning, O. Mehio, M. Buchhold, T. Kurumaji, G. Refael, J. G. Checkelsky, and D. Hsieh, *Signatures of ultrafast reversal of excitonic order in* Ta_2NiSe_5, Phys. Rev. Lett. **125**, 267602 (2020).

[50] H. Lang, O. Vendrell, and P. Hauke, *Generalized discrete truncated Wigner approximation for nonadiabatic quantum-classical dynamics*, J. Chem. Phys. **155**, 024111 (2021).

[51] O. Neufeld, J. Zhang, U. D. Giovannini, H. Hübener, and A. Rubio, *Probing phonon dynamics with multidimensional high harmonic carrier-envelope-phase spectroscopy*, Proc. Natl. Acad. Sci. U.S.A. **119**, e2204219119 (2022).

[52] U. De Giovannini, S. A. Sato, H. Hübener, and A. Rubio, *First-principles modelling for time-resolved ARPES under different pump–probe conditions*, J. Electron Spectrosc. Relat. Phenom. **254**, 147152 (2022).

[53] C. W. Nicholson, A. Lücke, W. G. Schmidt, M. Puppin, L. Rettig, R. Ernstorfer, and M. Wolf, *Beyond the molecular movie: Dynamics of bands and bonds during a photo-induced phase transition*, Science **362**, 821 (2018).

[54] T. Frigge, B. Hafke, T. Witte, B. Krenzer, C. Streubühr, A. Samad Syed, V. Mikšić Trontl, I. Avigo, P. Zhou, M. Ligges, D. von der Linde, U. Bovensiepen, M. Horn-von Hoegen, S. Wippermann, A. Lücke, S. Sanna, U. Gerstmann, and W. G. Schmidt, *Optically excited structural transition in atomic wires on surfaces at the quantum limit*, Nature (London) **544**, 207 (2017).

[55] J. Xu, D. Chen, and S. Meng, *Decoupled ultrafast electronic and structural phase transitions in photoexcited monoclinic* VO_2, Sci. Adv. **8**, eadd2392 (2022).

[56] S. W. Teitelbaum, T. Shin, J. W. Wolfson, Y.-H. Cheng, I. J. Porter, M. Kandyla, and K. A. Nelson, *Real-time observation of a coherent lattice transformation into a high-symmetry phase*, Phys. Rev. X **8**, 031081 (2018).

[57] M. Trigo, P. Giraldo-Gallo, M. E. Kozina, T. Henighan, M. P. Jiang, H. Liu, J. N. Clark, M. Chollet, J. M. Glownia, D. Zhu, T. Katayama, D. Leuenberger, P. S. Kirchmann, I. R. Fisher, Z. X. Shen, and D. A. Reis, *Coherent order parameter dynamics in* $SmTe_3$, Phys. Rev. B **99**, 104111 (2019).

[58] K. W. Stone, K. Gundogdu, D. B. Turner, X. Li, S. T. Cundiff, and K. A. Nelson, *Two-quantum 2D FT electronic spectroscopy of biexcitons in* GaAs *quantum wells*, Science **324**, 1169 (2009).

[59] R. Yusupov, T. Mertelj, V. V. Kabanov, S. Brazovskii, P. Kusar, J.-H. Chu, I. R. Fisher, and D. Mihailovic, *Coherent dynamics of macroscopic electronic order through a symmetry breaking transition*, Nat. Phys. **6**, 681 (2010).

[60] Y.-H. Cheng, F. Y. Gao, S. W. Teitelbaum, and K. A. Nelson, *Coherent control of optical phonons in bismuth*, Phys. Rev. B **96**, 134302 (2017).

[61] A. Zong *et al.*, *Dynamical slowing-down in an ultrafast photoinduced phase transition*, Phys. Rev. Lett. **123**, 097601 (2019).

[62] W. P. Su, J. R. Schrieffer, and A. J. Heeger, *Solitons in polyacetylene*, Phys. Rev. Lett. **42**, 1698 (1979).

[63] G. Paleari, F. Hébert, B. Cohen-Stead, K. Barros, R. T. Scalettar, and G. G. Batrouni, *Quantum Monte Carlo study of an anharmonic Holstein model*, Phys. Rev. B **103**, 195117 (2021).

[64] S. Li and S. Johnston, *The effects of non-linear electron-phonon interactions on superconductivity and charge-density-wave correlations*, Europhys. Lett. **109**, 27007 (2015).